UKAEA-CCFE-PR(20)06

Daniel R. Mason, Andrew J. London

Morphological analysis of 3d atom probe data using Minkowski functionals

Morphological analysis of 3d atom probe data using Minkowski functionals

Daniel R. Mason, Andrew J. London

This is a preprint of a paper submitted for publication in
Ultramicroscopy

Morphological analysis of 3d atom probe data using Minkowski functionals

Daniel R. Mason*
CCFE, UK Atomic Energy Authority, Culham Science Centre, Oxfordshire OX14 3DB, UK

Andrew J. London
CCFE, UK Atomic Energy Authority, Culham Science Centre, Oxfordshire OX14 3DB, UK

(Dated: June 21, 2019)

We present a morphological analysis of atom probe data of nanoscale microstructural features, using methods developed by the astrophysics community to describe the shape of superclusters of galaxies. We describe second-phase regions using Minkowski functionals, representing the regions' volume, surface area, mean curvature and Gaussian curvature. The alloy data in this work show microstructures that can be described as sponge-like, filament-like, and sphere-like at different concentration levels.

To enhance the accuracy of the analysis a maximum likelihood based denoising filter was developed. This filter performs significantly better than a simple Gaussian smoothing filter. We also interpolate the data using natural cubic splines, to refine voxel sizes and to refine the surface. We demonstrate that it is possible to find a mathematically well-defined, quantitative description of microstructure from atomistic datasets, to sub-voxel resolution, without user-tuneable parameters.

I. INTRODUCTION

Atom probe tomography (APT) [1–3] is a well-established technique for near-atomic resolution chemical characterization of metals. It offers a unrivalled window on chemical segregation in alloys, revealing nanometre scale precipitates, segregation of alloying elements or impurities to grain boundaries, and Cottrell atmospheres [4] where elastic interactions balance entropic penalties near dislocations. These features are often too small to be accurately quantified by transmission electron microscopy[5] or nanoSIMS[6], yet can determine the mobility of impurities or dislocation line segments[7, 8], and so are critical to understanding the kinetics of microstructural evolution, particularly systems far from equilibrium.

Due to its nature of identifying individual atoms, the signal from APT is inherently noisy. Identifying the location of a single impurity atom is of little significance, but it may be important to know, for example, where the carbon has segregated and its concentration is high. This paper aims to address such questions quantitatively using a simple mathematical description of microstructural morphology and topology, developed by the astrophysics community to describe the shapes of superclusters of galaxies[9] at MPc lengthscales (10^{22} m). This formalism uses the Minkowski functionals[10], and the associated 'shape-finder' functions[11], which allow a natural description of regions as sphere-like, plate-like, or ribbon-like. The general nature of the technique is proved by the application of Minkowski functionals to diverse fields- for example soil porosity[12] and medical imaging[13]- though we believe this is the first time they have been applied to atomistic datasets.

After briefly reviewing the mathematical formalism and the steps needed to find converged isosurfaces of concentration, we use simulated data to prove the power of the method to distinguish and quantify microstructural features. Then we use real atom probe data to find quantitative measurements of typical microstructural morphologies.

II. MINKOWSKI FUNCTIONALS AS SHAPE DESCRIPTORS

There are many ways to characterize microstructure, depending on the information available. Transmission electron microscopy might produce spatially varying strain information. Molecular dynamics or atomistic kinetic Monte Carlo might give potential energies. An APT experiment provides atom species and positions. In all these cases we can define a part of the microstructure as a spatial region which has a scalar property above some threshold value.

Consider a region in 3d space bounded by a closed surface. To start describing its shape we could report its volume. Then to give a second measure we could report its surface area. To go further in materials science is often done with *ad hoc* descriptors, for instance by reducing shapes to ellipsoids. But Hadwiger's theorem[14] tells us that in d-dimensional space there are in fact only $d+1$ descriptors which are invariant to translation and rotation , and which are additive and (conditionally) continuous. These are known as the Minkowski functionals. We can therefore describe microstructural morphology with just four functions.

If we have a continuous phase field $f(\vec{x})$, within which we have defined an isosurface S_f where $f(\vec{x}) = f$, then the four Minkowski functionals are commonly expressed

---

* daniel.mason@ukaea.uk

as V_0, V_1, V_2, and V_3, where the first,

$$V_0 = \frac{1}{3} \oint_{S_f} \vec{x} \cdot \hat{n} \, \mathrm{d}S, \tag{1}$$

where $\vec{x}$ is a position on the surface and $\hat{n}$ the local surface normal. This quantity is simply the volume enclosed by the surface, as can be readily seen by applying the divergence theorem. The second functional,

$$V_1 = \frac{1}{6} \oint_{S_f} \mathrm{d}S, \tag{2}$$

is proportional to the surface area. The third functional is

$$V_2 = \frac{1}{3\pi} \oint_{S_f} \frac{1}{2} \left(\frac{1}{R_1} + \frac{1}{R_2} \right) \mathrm{d}S, \tag{3}$$

where $R_{1,2}$ are the principal radii of curvature. V_2 is proportional to the integrated mean curvature, $C \equiv \oint_{S_f} \frac{1}{2} \left(\frac{1}{R_1} + \frac{1}{R_2} \right) \mathrm{d}S \equiv \oint_{S_f} H \mathrm{d}S$. The last functional is

$$V_3 = \frac{1}{4\pi} \oint_{S_f} \frac{1}{R_1 R_2} \mathrm{d}S \equiv \frac{1}{4\pi} \oint_{S_f} K \mathrm{d}S, \tag{4}$$

which is proportional to the integrated Gaussian curvature. V_3 is related to the genus, $g = 1 - V_3$, which is a count of the number of perforations through a solid - eg a sphere has $g = 0$, a figure 8 has $g = 2$ etc.

The mean curvature (H) and Gaussian curvature (K) of an implicit surface $f(\vec{x}) = f$ are given by [15]

$$H = \frac{\nabla f \cdot G \, \nabla f - |\nabla f|^2 \, \mathrm{Tr}\,(G)}{2 \, |\nabla f|^3}$$
$$K = \frac{\nabla f \cdot G^\star \, \nabla f}{|\nabla f|^4}, \tag{5}$$

where $G = \nabla \nabla f$ is a matrix of second derivatives, so that eg $G_{xy} = \frac{\partial^2 f}{\partial x \partial y}$, and $G^\star$ a matrix of the cofactors of G, so that eg $G^\star_{xy} = \mathrm{Cofactor}(G_{xy}) = G_{yz} G_{zx} - G_{yx} G_{zz}$. We can therefore compute the surface integrals, equations 1-4, as a discrete sum by first making a polyhedral surface, and using its faces as the area elements.

There is a second, very quick, and exact method[16] for computing the integrated Gaussian curvature via the Euler characteristic, χ. For any polyhedron this can be found by counting the number of vertices, edges and faces.

$$\chi = 2 V_3 = N_{\text{vertices}} - N_{\text{edges}} + N_{\text{faces}}. \tag{6}$$

We can also find an approximation for the mean curvature C from a triangulated surface[16]. If two triangles with normals $\hat{n}_1$ and $\hat{n}_2$ share an edge of length x, then

$$C = \frac{1}{2} \sum_{\text{edges}} \varepsilon x \phi, \tag{7}$$

where $\cos \phi = \hat{n}_1 \cdot \hat{n}_2$ and $\varepsilon = \pm 1$ depending on whether the vectors drawn through the centroids of the triangles in the direction of the normals have their closest approach within the surface ($\varepsilon = +1$) or outside ($\varepsilon = -1$). This method is robust for large shapes described by many triangles, but inaccurate in the limit of regions bounded by a few triangles with a high angle between normals.

We can describe a surface using a triangulated mesh, and hence maintain a working estimator for the errors in the Gaussian and mean curvatures of the surface by comparing equations 6 and 7 with equations 5, and refine the surface mesh by adding triangles until these errors are acceptable, using the method in section VIII B. In the figures shown in this paper, the genus is computed using 6 and the mean curvature from 7.

III. SHAPEFINDERS

From the four Minkowski functionals we can define 'shapefinder' functions[11],

$$S_1 = \frac{V_0}{2 V_1}, \quad S_2 = \frac{2 V_1}{\pi V_2}, \quad S_3 = \frac{3 V_2}{4}. \tag{8}$$

These three functions have dimensions of length and are normalised to return $S_i = R$ for a sphere of radius R. For a convex surface $S_1 \le S_2 \le S_3$. From these a further two shapefinders can be defined[11]

$$T_1 = \frac{S_2 - S_1}{S_2 + S_1}, \quad T_2 = \frac{S_3 - S_2}{S_3 + S_2} \tag{9}$$

which can be used to distinguish shapes. For a spheroid, $T_1 \simeq T_2 \simeq 0$. A filament has $T_1 \ll T_2 \simeq 1$. A ribbon has $T_1 \simeq T_2 \simeq 1$. A pancake has $T_2 \ll T_1 \simeq 1$.

IV. COMPUTING MINKOWSKI FUNCTIONALS FROM DISCRETE DATA

Atom probe data, or indeed molecular dynamics data, consists of a large dataset of discrete points $\{\mathrm{type}_i, x_i, y_i, z_i\}$, for $i = \{1, 2, ..\}$. To use Minkowski functionals with atomic position data, we need to first define isosurfaces within this data, which in turn requires a continuous function, $f(\vec{x})$. This is generally done as a two-stage process. First, atoms are assigned to voxels. The count of atoms of a given type within a voxel is converted to a value of concentration, defined at a node point in the centre of the voxel. The voxel size is a tuneable parameter for the interpretation of the data, but it must lie within narrow bounds: if voxels are too small, there will be too few atoms counted per voxel and the concentration at nodes will be very noisy. If the voxels are too large, then spatial variations will be averaged over[17, 18].

Once the atomic position data is presented as concentrations on discrete node points, $\{f(l, m, n)\}$, it is necessary to find a continuous interpolating function $f(\vec{x})$

within which we can define an isosurface. Our strategy is based on two observations. Firstly atomistic data is generally used to describe nano-scale systems, and so clusters are rather small, only a few nanometres across. But voxels need to be of order 1 nm to contain enough atoms to produce sensible mean quantities. We therefore need a method with sub-voxel resolution. Secondly we note that a voxel of side length a by its nature must have a limiting spatial scale a for variations in concentration, and so it can only properly be used to describe a field that is smooth at this scale.

We use the marching cubes algorithm[19] to find a triangulated isosurfaces. This uses a computationally efficient trilinear interpolation between node values. But as we need an interpolation with continuous zeroth, first and second derivatives of $f(\vec{x})$ to find the curvatures in equation 5, we employ a complementary natural tricubic spline interpolation for $f(\vec{x})$ and its derivatives, and push the marching cubes vertices to a from linear interpolated points to the cubic-interpolated surface (see section VIII B).

When placing atoms into voxels, we may treat them as having a finite Gaussian delocalisation width σ_a. If $\sigma_a > 0$, then each atom will in fact be placed in a local region of voxels, with weighting given by the distance from atom to node divided by σ_a. After each atom is placed in one or more voxels, we could then apply a Gaussian smoothing with kernel width σ_v to the concentration on the nodes.

Figure 1 shows the importance of denoising and mesh refinement as a preliminary step for analysing the morphology and topology of microstructure. We see that if atoms are placed onto voxels with no delocalisation and no smoothing of the concentration data, then a very large number of distinct isosurfaces are found, where the noisy signal happens to pass threshold. This noise appears as small octahedral isosurfaces centred on the underlying voxel lattice points. If the atoms are delocalised, or the concentration values on the voxels are smeared with a Gaussian filter, then the noise is reduced, but at the expense of modifiying the concentration profile.

We start our method with a small Gaussian atom delocalisation and zero voxel smearing, $\sigma_a = a/2, \sigma_v = 0$. We then use a maximum likelihood denoising filter described in section VIII A to remove noise but preserving atom count and not unduly distorting the concentration. We then increase the voxel count by halving the spacing between voxel nodes, using a tricubic interpolation of the concentration values. This helps the Marching Cubes algorithm find a topologically robust surface. Finally we apply the denoising filter to the refined voxels.

Figure 2 shows that a broad delocalisation $\sigma_a = a$, or smearing $\sigma_v = a$ do an equally good job reproducing the isosurface of a soft inclusion at low concentration, but tend to smooth out the corners of the hard inclusion. A smaller kernel width $\sigma_a = a/2$, or $\sigma_v = a/2$ do better at higher concentrations, with atom smearing appearing to be preferable. Our maximum likelihood denoising filter and mesh refinement performs well in both cases.

Also on figure 2 we plot the proxigram[21] of concentration vs distance, as computed using IVAS[22] with the same atomic dataset. The proxigram uses the distance of atoms from a single fixed isosurface (here we chose $f = 0.4$), so in fact reports the concentration as a dependent variable with distance as the abscissa. Here we have exchanged the axes, and also offset the position of the interface to make a clearer comparison to the shapefinders used here. The proxigram does a better job of finding the concentration gradient at this isolevel than our denoising filter, especially in case of a hard interface, as it works from the original atomic data rather than voxels. It does, however, show considerable scatter far from its fixed isosurface, where the inclusion is small and there are fewer atom counts. The time taken for both methods is similar as both scale linearly with system size.

Figure 3 shows the convergence of our method with the resolution of the voxel grid size, a, and with the atom count per voxel, ρ. The same soft inclusion with characteristic Gaussian profile (described in section V) is used. We conclude that particles with a diameter twice the voxel spacing are readily resolved, and when they have four times the voxel spacing their concentration profile is resolved to high accuracy. We see that the inclusion is recognised when the voxels have only 5 atoms each, and is well resolved when voxels contain 20 atoms. We also conclude that our maximum likelihood denoising algorithm is significantly better than Gaussian smoothing. In figure 3 we also compare to the established literature method of computing Minkowski functionals using counting of faces,edges and vertices of the voxels over threshold[23]. This method uses a fixed set of normals to describe the surface, and so while the method converges, and the four Minkowski functionals give a characteristic ‘fingerprint’ with which to distinguish microstructures, the area (and hence the shapefinders) can not generally converge to the correct values[24].

V. MODEL CASES

In this section we apply the formalism to construct the shape-finder functions for simple model cases, and demonstrate the ease with which it is possible to distinguish microstructural objects.

The model systems are constructed by placing atoms randomly into a box of side $L = 40$ nm, at a density 20 atoms/nm^3. Each atom is randomly determined to be of type ‘A’ or ‘B’, with a probability of selecting ‘B’ equal to the local concentration, defined by an analytic expression. The discrete data was placed into voxels of size $a = 1$ nm, denoised with the MLD filter, the voxel spacing refined to $a/2$ nm, then denoised a second time as described above. Figure 4 shows isosurfaces of a model system containing a single toroidal inclusion defined below. The background level is set to 10% concentration of type ‘B’. We see that at the 5% concentration level there are negative spaces- holes- inside the enclosing surface,

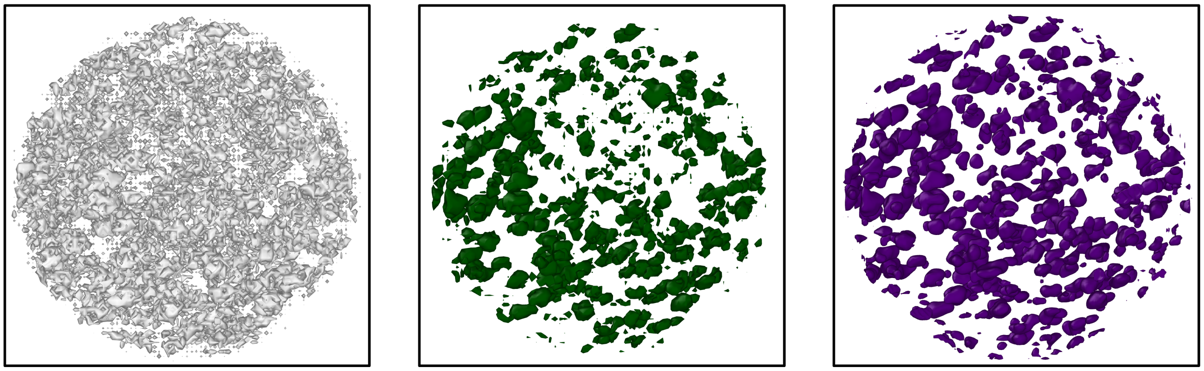

FIG. 1. Renderings of the same atom probe data of an inconel sample[20], rendered at a (Nb+Ti) concentration $f = 10\%$, with increasing levels of denoising. Left-to-right: i) Atom data as received, placed on voxels ($a = 1.0$ nm) with no delocalisation. ii) Atoms delocalised by $\sigma_a = a/2$, then voxels smeared with $\sigma_v = a/2$. iii) Atoms delocalised by $\sigma_a = a/2$, voxel node spacing halved, then max likelihood denoising filter applied.

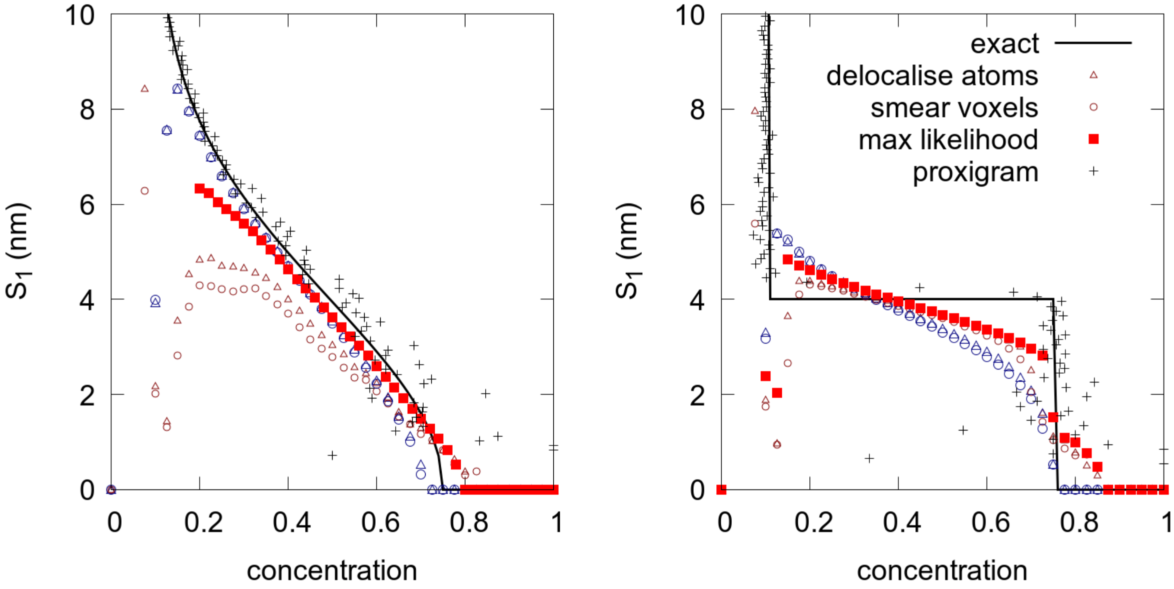

FIG. 2. A comparison of methods for smoothing the voxel field. Atoms placed in voxels side $a = 1$nm, with (left) a Gaussian profile inclusion $f(\mathbf{r}) = f_0 + f_1 \exp(-|\mathbf{r}|^2/2\sigma^2)$, and (right) a top hat inclusion $f(\mathbf{r}) = f_0 + f_1 H(\sigma - r)$, with $f_0, f_1 = 0.1, 0.65$, and $\sigma = 4$nm. Average 20 atoms per voxel. Open triangles: atoms smeared using a Gaussian kernel of $\sigma_a = a/2$ (small red) or $\sigma_a = a$ (large blue) , so each atom is added to multiple voxels. open circles: atoms placed in nearest voxel only, then concentration field smeared with a Gaussian kernel with $\sigma_v = a/2$ (small red) or $\sigma_v = a$ (large blue) afterwards. Filled squares: atoms smeared using a Gaussian kernel of $\sigma_g = a/2$, then the maximum likelihood filter described here applied. Plusses: computation using IVAS[22] with the proxigram method[21] centred on an isosurface at $f = 0.4$. Note that this method uses the original atom positions, so has a more accurate description of the concentration gradient near $f = 0.4$.

and at 15% concentration level there are convex shapes - these are complementary topologies. At a 75% concentration level the torus appears rather thin, as voxels which just graze the toroidal surface are unlikely to contain a high concentration. At the highest level the torus appears to break up- few voxels have 80% concentration or above and they are not contiguous.

The defect shapes we consider are:

1. "Random solid solution" - the analytic concentration is fixed at $f(\mathbf{x}) = 50\%$, and we look for the effect of the random sampling of atoms only. In figure 5 we see that the genus spikes at the background concentration, as voxels are equally likely to be above or below threshold. The topology is that of a sponge. In out example cases below, the background level is at $f = 10\%$, and the same genus spike can be seen in each.

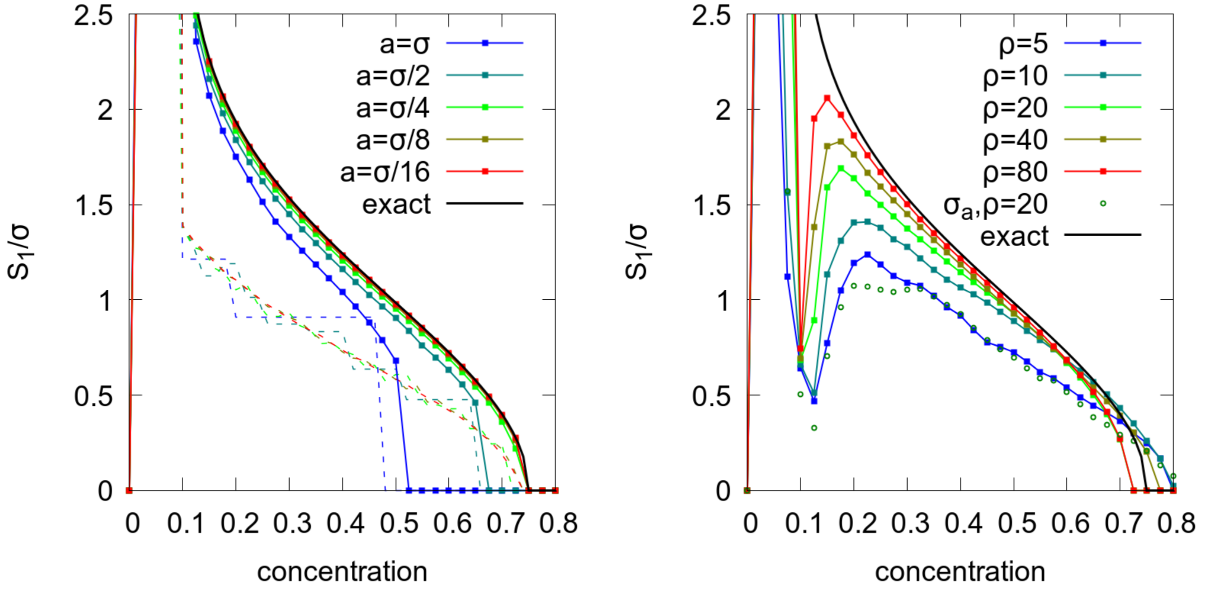

FIG. 3. A demonstration of the convergence of the method described here to the analytical solution. Left: convergence with increasing voxel resolution. The analytical voxelised concentration field for a Gaussian inclusion is used as input, with the voxel side length varying from the Gaussian standard deviation $\sigma/16$ to σ. Solid lines: the method described here using Marching Cubes to triangulate the surface and the maximum likelihood denoising algorithm in appendix VIII A. Dashed lines: the vertex-counting method described in ref[23]. Right: convergence with atom density, ρ, placing atoms in voxels size $a = \sigma/4$. The concentration field for a Gaussian inclusion is used as input, but starting with randomly positioned atoms instead of an analytic function. The expected number of atoms per voxel is increased from 5 to 80. the method described here using Marching Cubes to triangulate the surface and the MLD algorithm. Open circles are the result using Marching Cubes to triangulate the surface but with an atomic delocalisation using $\sigma_a = a/2$.

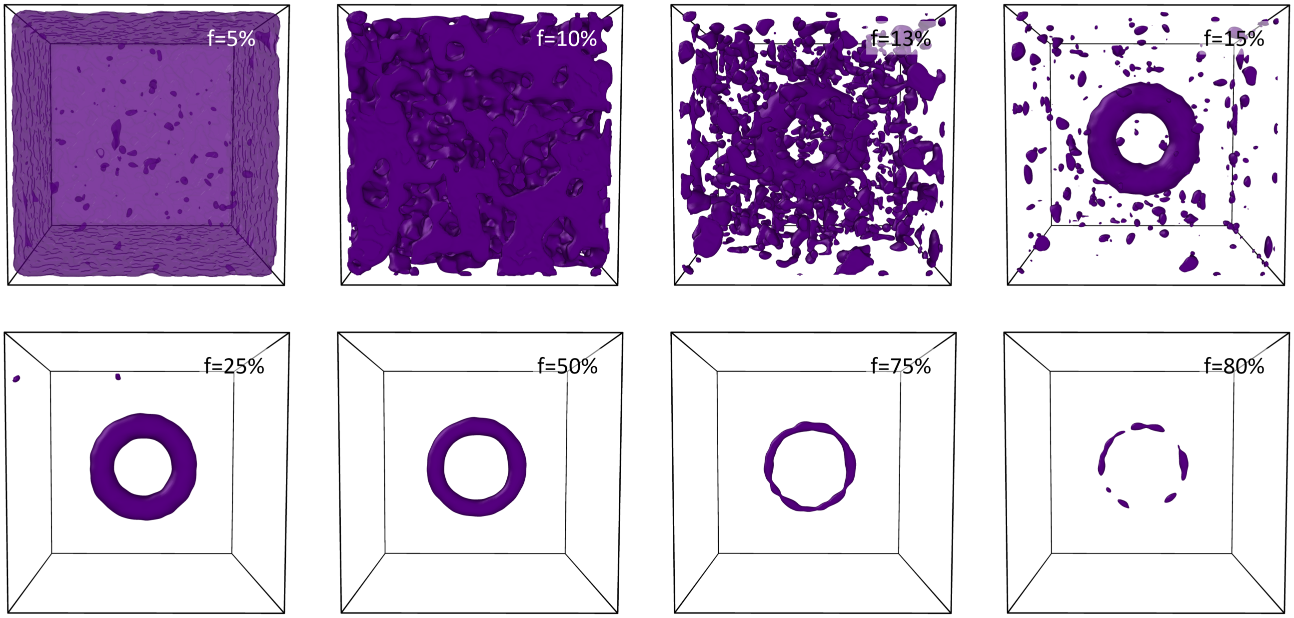

FIG. 4. Renderings of the toroidal isosurfaces constructed from randomly generated noisy voxels, illustrating features common to concentration isosurfaces. The top-left surface is drawn with some transparency. The background concentration is 10%, within the torus it is 75%. Left-to-right and top-to-bottom, the concentration levels are 5%,10%,13%,15%, 25%,50%,75%,80%. At around the background level, there is a complex sponge-like topology, with some regions above and some below the average concentration. The 50% concentration isosurface shows a perfect torus, but it is important to note that a full description of the microstructure should be of all eight images, not just this 'good-looking' one.

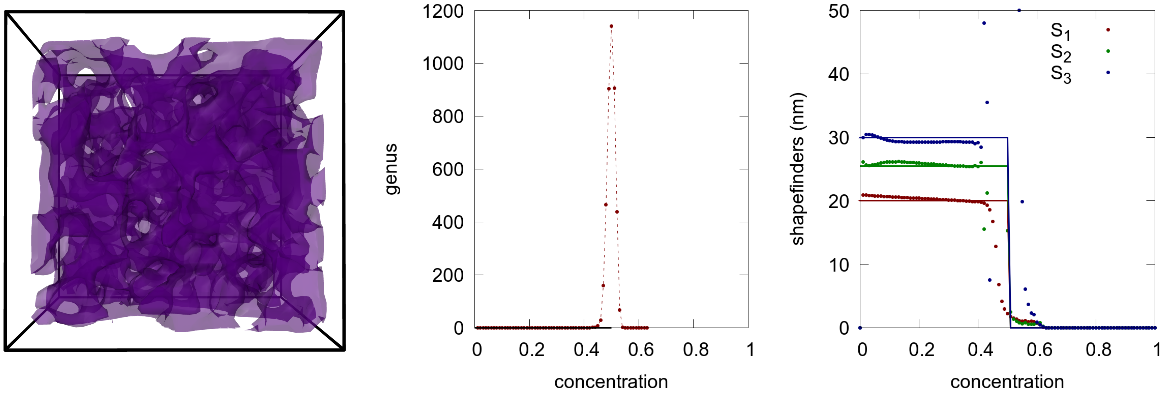

FIG. 5. A demonstration using a random solid solution at concentration level $f = 50\%$. Left: the 50% concentration isosurface rendered with some transparency shows a characteristic sponge-like topology (cf the toroidal inclusion figure 4 at f=10%).

2. "Hard interface inclusion" - has a top hat concentration profile

$$f(\mathbf{r}) = f_0 + f_1\Theta(\sigma - |\mathbf{r}|), \tag{10}$$

   where $\Theta(x)$ is the Heaviside function. $\mathbf{r}$ is the vector separation from the centre of the box, and $\sigma = 4$nm. The background concentration takes value $f_0 = 10\%$, and the centre of the inclusion $f_0 + f_1 = 75\%$. In figure 6, we see that the genus is zero, indicating a solid object with no piercings. The shapefinders s_1, s_2, s_3 are equal over the concentration range, indicating a spherical object, but they vary by about 1 nm over the range owing to the finite resolution of the voxelised representation of the concentrations. This is the limiting accuracy of using voxels do describe a hard interface. In this figure, and the remaining models in this section, we render the isosurface at $f = 35\%$ using Ovito [25][1]

3. "Soft interface inclusion" - has a Gaussian concentration profile

$$f(\mathbf{r}) = f_0 + f_1 \exp(-\frac{|\mathbf{r}|^2}{2\sigma^2}), \tag{11}$$

   The constants take the same values as the hard interface inclusion. See figure 7. Again we see a genus zero spherical object, but here there is a large variation in the characteristic lengths s_1, s_2, s_3, matching the radius r of the inclusion at concentration $f(r)$.

4. "Segregation to dislocation line" - has a concentration profile centred on a wavy line

$$f(\mathbf{r}) = f_0 + f_1\Theta(\sigma - x), \tag{12}$$

   where x is the minimum distance to a sinusoidal line defined by $\mathbf{r}(\lambda) = L/2\lambda\hat{z} + \sigma\sin(2\pi\lambda)\hat{x}$, with $-1 \leq \lambda \leq 1$. See figure 8. This object is seen to be genus zero again, but non-spherical- here $s_3 >> s_1 \simeq s_2$ and so we recognise a filament-like object.

5. "Dislocation loop" - has a toroidal concentration profile

$$f(\mathbf{r}) = f_0 + f_1\Theta(\sigma/2 - x), \tag{13}$$

   where x is the minimum distance to a ring with radius 8nm. See figure 9. The shapefinders s_i look very similar to the previous case, but this time the genus is one, indicating an object pierced with one hole.

We see that we can distinguish these model cases at a glance, and the morphological and topological data presented in figures 5 to 9 have a quantitative and intuitive meaning.

VI. 3D ATOM PROBE DATA

A. Atom Probe Analyses

Atom probe tomography was performed on four materials: an age-hardened CuCrZr alloy [27], and Inconel [20], ion-irradiated EUROFER97 steel [28], and a NbTi superconducting alloy [29], A LEAP 3000X HR (Imago, USA) was used with following parameters to maintain field evaporation: 532 nm laser with 0.5 nJ pulse energy, 200 kHz repetition rate, a 0.2% evaporation rate and 50 K specimen temperature.

In real atom probe data there may be multiple closed isosurfaces at a concentration level f. These isosurfaces naturally divide the system into regions, without any requirement to find clusters in the data[30]. The method described here will report each isosurface (and therefore each distinct microstructural feature) individually, but

---

[1] Note that Ovito uses Gouraud shading[26] to make the surface appear smoother.

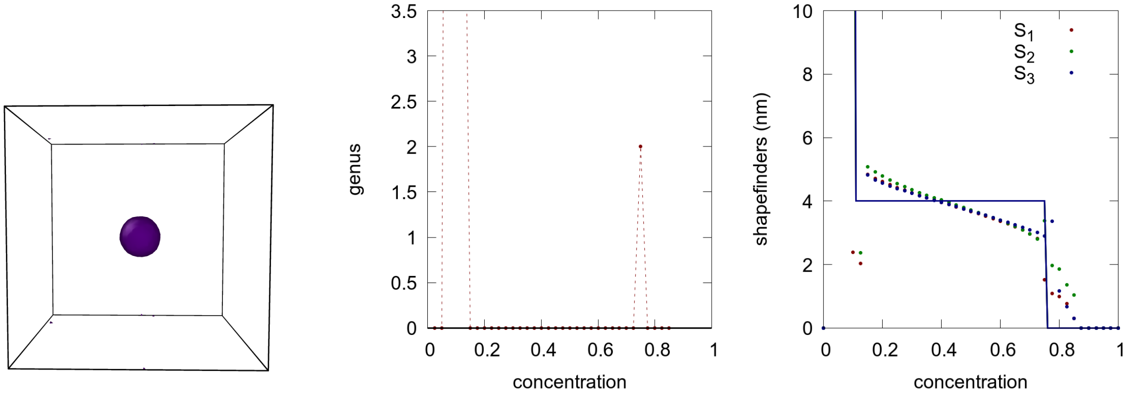

FIG. 6. A demonstration using a hard interface inclusion, defined with a top hat profile. Left: a rendering of the isosurface at $f = 35\%$[25]. Right: The computed genus and shapefinders for the isosurface containing the largest volume computed from the noisy voxels. Solid lines indicate the analytical values at infinite atom count and infinitessimal voxel size. Note that the genus is zero over nearly all the concentration range, indicating a solid object without piercings. However at the limiting concentration the shapefinders have scatter. This is characteristic behaviour of the concentration isosurface breaking up. The shapefinders vary by about 1 nm over the concentration range. This is a limitation of placing atoms into voxels of side 1 nm.

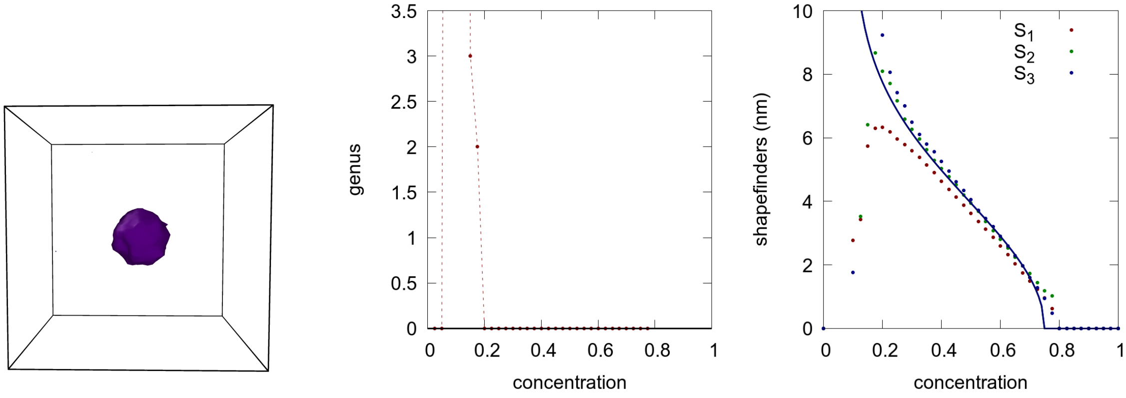

FIG. 7. A demonstration using a soft interface inclusion, defined with a Gaussian profile. As for figure 6, the genus is low, indicating a solid object without piercings. The shapefinders vary considerably over the concentration range, matching the radius of the object, and clearly dissimilar to the hard-sphere object in figure 6. Note that the shapefinders are measures of characteristic distance - at a concentration just over background when largest isosurface starts to percolate through the system, and the smallest and largest characteristic dimensions diverge.

for conciseness of the exposition, we present data averaged over individual isosurfaces.

For a number of distinct isosurfaces, n_{iso}, we can identify two populations. Some will have the concentration gradient, ∇f, pointing into the surface. These can be described as having a positive volume. The number density of these is a measure of the number density of inclusions with at least this concentration. Other isosurfaces will have the concentration gradient pointing out of the surface. These are empty spaces in the microstructure, and can be said to have negative volume. In figures 10 to 13 we report the number density of positive and negative volume isosurfaces. We also use the normalised shapefinder $S_3 = 3V_2/(4n_{iso}$, which is directly comparable to S_1 and S_2.

For our atom probe examples, isosurfaces containing a (absolute) volume less than $(\pi a^3/2)$ were excluded from the summations, as a feature must cover more than one voxel to provide reliable shape information.

The CuCrZr alloy example is shown in figure 10. Atoms were placed in voxels of size $a = 1$nm, before denoising and refinement. We report the morphology of the Cr isosurfaces. We see that the genus is almost zero-none of the Cr inclusions are pierced, though there are a couple of excursions where the isosurfaces touch. The number density steadily falls with concentration, showing the inclusions have different peak concentrations. The shapefinders prove the inclusions are small, with a diameter of a few nanometres, and of fairly regular spherical shape as $T_1 \simeq T_2 \simeq 0$. Cr-rich regions with at least 25% Cr have an average radius $\langle S_1 \rangle = 1.7 \pm 0.1$ nm, and the population has a standard deviation 0.6 nm.

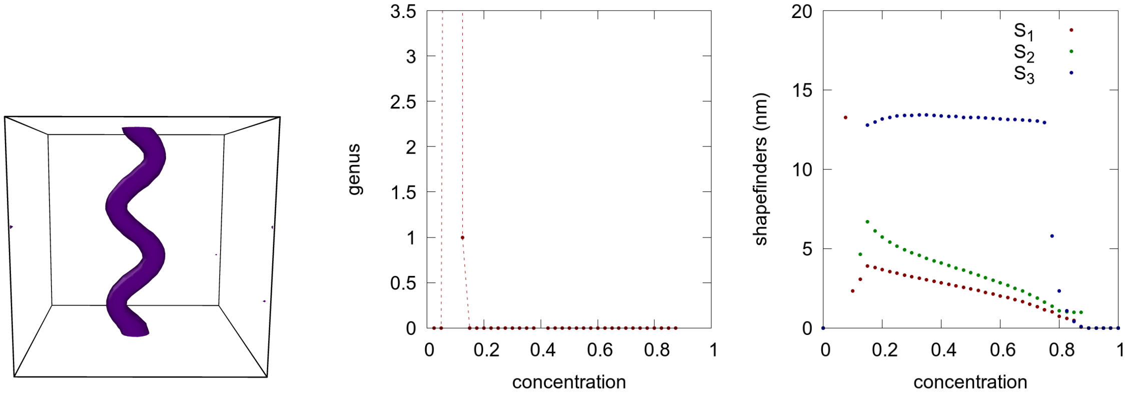

FIG. 8. A demonstration using segregation to a dislocation line, defined with a sinusoidal profile. Left: a rendering of the isosurface at $f = 35\%$[25]. Right: The computed genus and shapefinders for the isosurface containing the largest volume computed from the noisy voxels. Note that the shapefinders, indicative of the dimensions of the object, are dissimilar to the inclusions in figures 6 and 7 - one dimension is much greater than the other two.

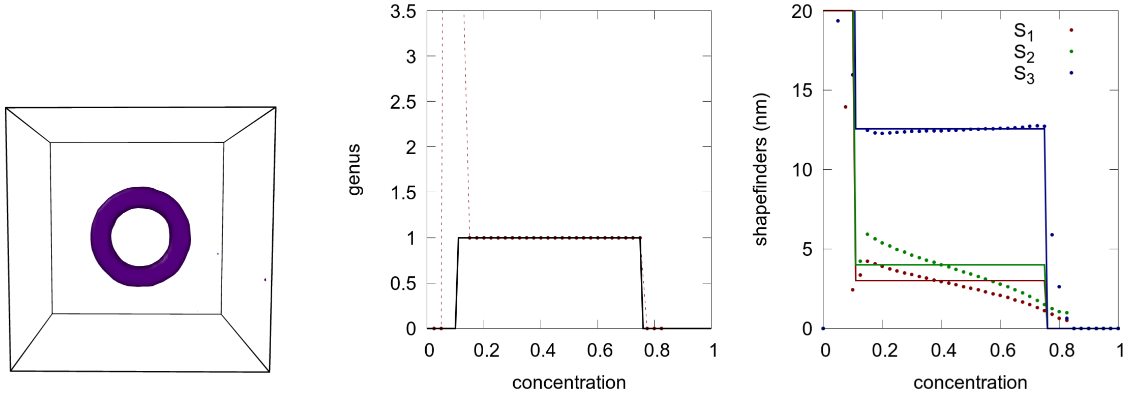

FIG. 9. A demonstration using segregation to a dislocation loop inclusion, defined with a toroidal profile. Left: a rendering of the isosurface at $f = 35\%$[25]. Right: The computed genus and shapefinders for the isosurface containing the largest volume computed from the noisy voxels. Solid lines indicate the analytical values. Note that the shapefinders, indicative of the dimensions of the object, look similar to the dislocation line in figure 8, but the genus is one, indicating a shape with a single hole through it.

The inconel example is shown in figure 11. Atoms were placed in voxels initially of size $a = 1.5$nm, and we report isosurfaces of the combined concentration of Nb and Ti. We see that the genus peaks at a concentration of 7%- this somewhat unexpected result is due to a tube containing very low concentration- probably a zone line- running the length of the needle and cutting though several precipitates. This zone line is indicated by the arrows in figure 11. Though not easily seen in isosurface renderings, it is directly apparent in the genus, and shows that further analysis of this sample should account for this region. The number density shows that there is a characteristic concentration, around 10%, but that at 5% concentration the isosurfaces start to connect together. The shapefinders prove the inclusions are not spherical, $T_1 \simeq T_2 \neq 0$, and considerably larger than those in the Cu-Cr example. Regions with a combined Nb+Ti concentration over 6% have a minor(major) size $\langle S_1 \rangle = 4.3 \pm 0.3$ nm, ($\langle S_3 \rangle = 9.2 \pm 1.0$ nm), with a population standard deviations 2.5 nm (7.1 nm).

We show Mn segregation in irradiated Eurofer steel in figure 12. Atoms were placed in voxels initially of size $a = 1.5$ nm. The average Mn concentration is 0.45%. At this level we see a peak in genus and a drop in the number density. At around just above 0.45% concentration we conclude that the Mn is distributed as a filamentary web- long thin strings of Mn which are likely following dislocation lines. At higher concentration, 1% Mn, it is considerably easier to recognise these lines in a rendering of the isosurfaces, and their filamentary character is confirmed by the shapefinders ($T_1 > T_2$), but the isosurfaces are starting to break up, indicating that the Mn is not evenly distributed at this concentration. The average values are strongly affected by the presence of a large number of small, spherical regions where Mn has segregated, possibly to small irradiation-induced defects.

Figure 13 shows an analysis of Ti concentration isosurfaces in a NbTi superconducting alloy. Atoms were placed in voxels initially of size $a = 1.5$nm. The rendering shows two distinct regions, of high Ti,low Nb, and of higher Nb, lower Ti. The average Ti concentration in the needle as a whole is 65%, but we see the peak in genus at a somewhat lower level, closer to 55%, which is the concentration in the high Nb region. The shapefinders show that the high 80% Ti regions are large and plate-like ($T2 > T1$).

VII. CONCLUSION

In this paper we have described the use of shapefinder functions to describe the morphology of atom probe samples. In section IV, we found that our use of a tricubic interpolation for mesh refinement and a maximum likelihood denoising filter enabled highly accurate sub-voxel resolution for the sizes of inclusions. In particular we found that a good estimate for the concentration profile was possible even where the voxel size to the inclusion size, and that only ten to twenty atoms per voxel are required. This is a significant improvement on the standard use of Gaussian smoothing kernels.

Regions of interest are naturally separated into discrete isosurfaces, with no need to find clusters in the data, but at a lower concentration isolevel where the tails of the distributions of clusters overlap we see the merging of isosurfaces and the development of a sponge-like topology. We have shown that distinguishing typical microstructural features can be done at a glance from the shapefinders and genus, and that intuitive measures for their size and shape are computed quantitatively.

This paper has focussed on concentration data in atom probe needles, but the same techniques apply without modification to any atomistic dataset and any scalar field.

ACKNOWLEDGMENTS

This work has been carried out within the framework of the EUROfusion Consortium and has been received funding from Euratom research and training programme 2019-2020 under grant agreement No. 633053 and from the RCUK Energy Programme [grant number EP/P012450/1]. The views and opinions expressed herein do not necessarily reflect those of the European Commission. The authors would like to thank Sergei Dudarev, CCFE for helpful discussions and Paul Bagot, Oxford University, for providing the Inconel atom probe data set.

---

[1] Baptiste Gault, Michael P. Moody, Julie M. Cairney, and Simon P. Ringer. *Atom Probe Microscopy.* Springer New York, 2012.

[2] T.F. Kelly and M.K. Miller. Invited review article: Atom probe tomography. *Rev. Sci. Instrum.*, 78:031101, 2007.

[3] D.N. Seidman. Three-dimensional atom-probe tomography: Advances and applications. *Ann. Rev. Mat. Res.*, 37:127–158, 2007.

[4] A.H. Cottrell and B.A Bilby. Dislocation theory of yielding and strain ageing of iron. *Proc. Phys. Soc. A*, 62:49, 1949.

[5] M.A. Kirk, X. Yi, and M.L. Jenkins. Characterization of irradiation defect structures and densities by transmission electron microscopy. *Journal of Materials Research*, 30(9):1195–1201, 2015.

[6] J. Nuñez, R. Renslow, J. B. Cliff, and C.R. Anderton. Nanosims for biological applications: Current practices and analyses. *Biointerphases*, 13(3):03B301, 2018.

[7] T. D. Swinburne and S. L. Dudarev. Kink-limited orowan strengthening explains the brittle to ductile transition of irradiated and unirradiated bcc metals. *Phys. Rev. Materials*, 2:073608, Jul 2018.

[8] Thomas Nogaret and David Rodney. Finite-size effects in dislocation glide through random arrays of obstacles: Line tension simulations. *Phys. Rev. B*, 74:134110, Oct 2006.

[9] Einasto, M., Saar, E., Liivamägi, L. J., Einasto, J., Tago, E., Martínez, V. J., Starck, J.-L., Müller, V., Heinämäki, P., Nurmi, P., Gramann, M., and Hütsi, G. The richest superclusters - i. morphology. *A&A*, 476(2):697–711, 2007.

[10] J. Schmalzing, M. Kerscher, and T. Buchert. Minkowski functionals in cosmology. *Proc. Int. Sch. Phys. Fermi*, 132:281–291, 1996.

[11] Varun Sahni, B. S. Sathyaprakash, and Sergei F. Shandarin. Shapefinders: A new shape diagnostic for large-scale structure. *The Astrophysical Journal*, 495(1):L5–L8, mar 1998.

[12] F San José Martinez, L. Martin, and Garcia-Gutíerrez. Minkowski functionals of connected soil porosity as indicators of soil tillage and depth. *Front. Environ. Sci.*, 6:55, 2018.

[13] X. Li, P.R.S. Mendonça, and R. Bhotika. Texture analysis using minkowski functionals. *Proc. Medical Imaging 2012: Image processing*, 8314:83144Y, 2012.

[14] H Hadwiger. *Vorlesungen Uber Inhalt, Oberfl ache und Isoperimetrie.* Springer Verlag, Berlin Heidelberg, 1975.

[15] R. Goldman. Curvature formulas for implicit curves and surfaces. *Comp. Aided Geom. Design.*, 22:632–658, 2005.

[16] J.V. Sheth, V. Sahni, S.F. Shandarin, and B.S. Sathyaprakash. Measuring the geometry and topology of large-scale structure using surfgen: methodology and preliminary results. *Mon. Not. R. Astron. Soc.*, 343:22–46, 2003.

[17] M. G. HETHERINGTON and M. K. MILLER. Some aspects of the measurement of composition in the atom probe. *Le Journal de Physique Colloques*, 50(C8):C8–535–C8–540, November 1989.

[18] K.L. Torres, M. Daniil, M.A. Willard, and G.B. Thompson. The influence of voxel size on atom probe tomogra-

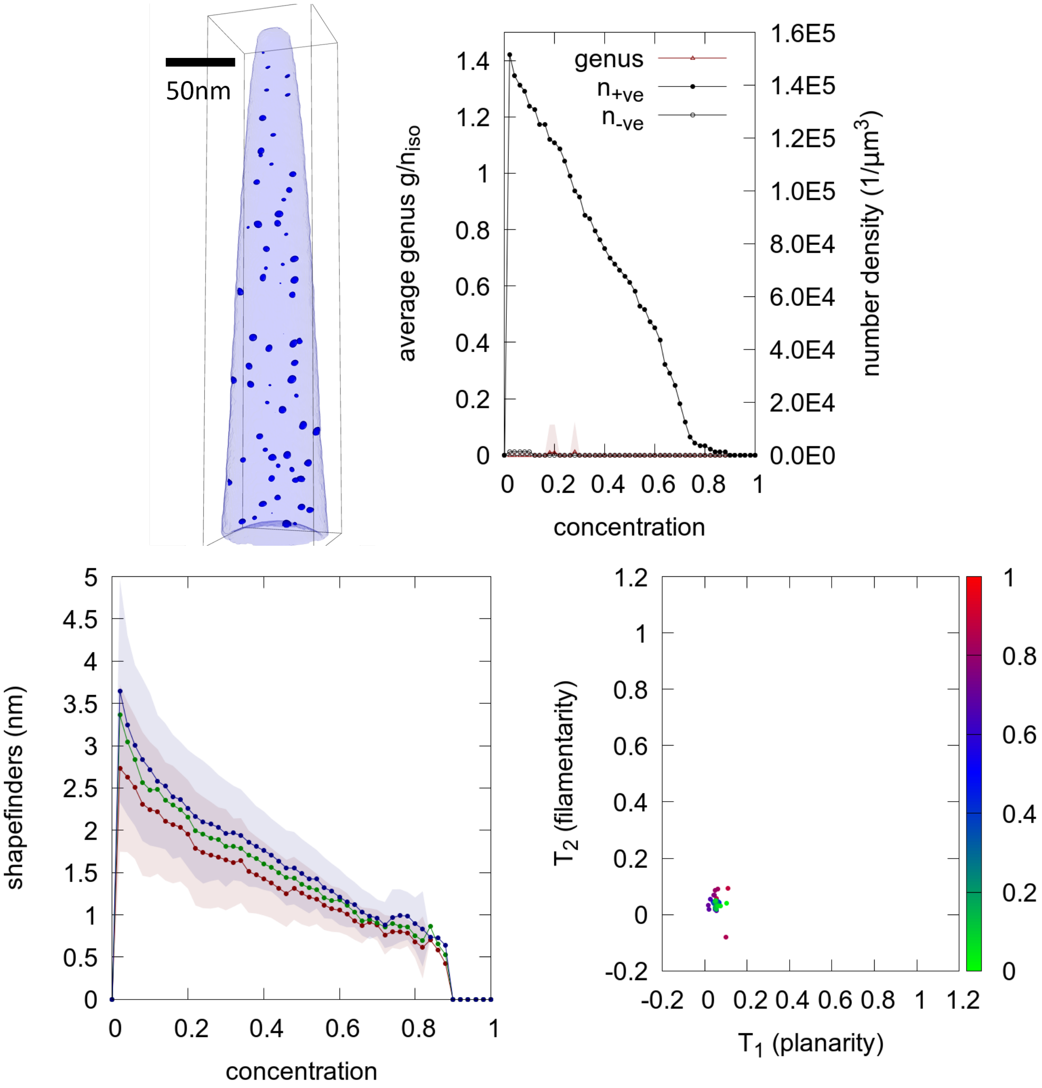

FIG. 10. A rendering of the isosurface at $f = 25\%$Cr [25] showing roughly spherical inclusions. At any given concentration there may be zero, one, or many separate isosurfaces. We can therefore plot quantities for the system as a whole, or averaged over isosurfaces. The four panels show i) A rendering of the isosurface at $f = 25\%$Cr [25] showing roughly spherical inclusions. ii) the average genus, together with an error bar taken from the standard deviation of the genus of separate isosurfaces, and the number density of surfaces containing both negative and positive volumes. iii) the shapefinders S_i - taken as averages over separate isosurfaces. The error bars are taken from the standard deviation of separate isosurfaces. iv) the shapefinders T_i computed from the average S_i.

phy data. *Ultramicroscopy*, 111(6):464–468, May 2011.

[19] Thomas Lewiner, Hélio Lopes, Antônio Wilson Vieira, and Geovan Tavares. Efficient implementation of marching cubes' cases with topological guarantees. *J. Graphics, GPU, & Game Tools*, 8:1–15, 2003.

[20] Hazel Gardner, Stella Pedrazzini, James O. Douglas, Didier De Lille, Michael P. Moody, and Paul A. J. Bagot. Atom probe tomography investigations of microstructural evolution in an aged nickel superalloy for exhaust applications. *Metallurgical and Materials Transactions A*, 50(4):1862–1872, Apr 2019.

[21] Olof C. Hellman, Justin A. Vandenbroucke, Järg Rüsing, Dieter Isheim, and David N. Seidman. Analysis of three-dimensional atom-probe data by the proximity histogram. *Microscopy and Microanalysis*, 6(05):437–444, September 2000.

[22] CAMECA. *Atom probe tomography.* AMETEK Materials analysis division, 2017.

[23] K. Michielsen and H. De Raedt. Integral-geometry morphological image analysis. *Phys. Rep.*, 347:461–538, 2001.

[24] J. Koplowitz. Design of perimeter estimators for digitized planar shapes. *IEEE Trans. Pattern Analysis and Machine Intelligence*, 11:611, 1989.

[25] A. Stukowski. Visualization and analysis of atomistic simulation data with OVITO - the open visualization tool. *Model. Simul. Mater. Sci. Eng*, 18:015012, 2010.

[26] H. Gouraud. Continuous shading of curved surfaces. *IEEE Trans. Computers*, C-20(6):623–629, 1971.

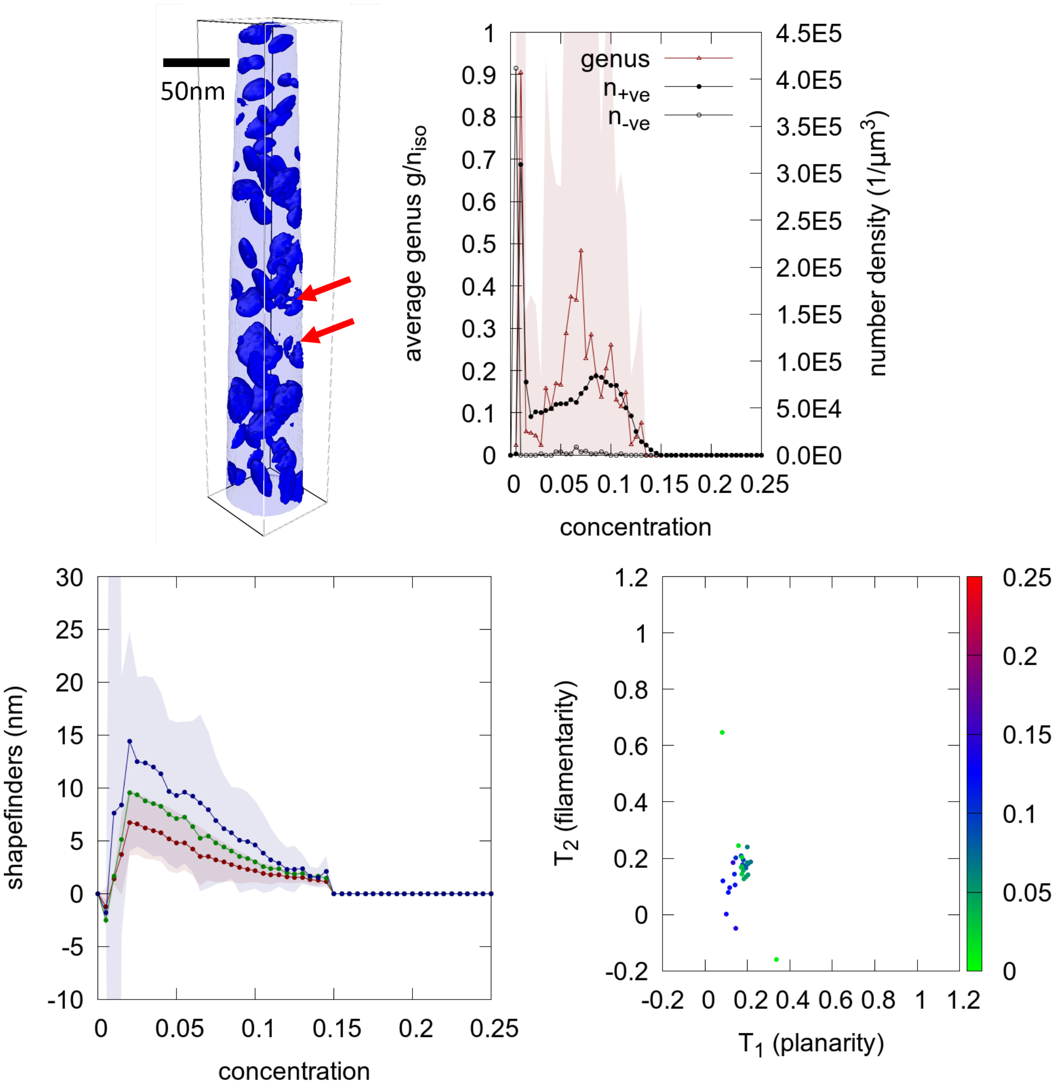

FIG. 11. An analysis of the combined Nb+Ti concentration isosurfaces in an inconel needle. The isosurface is rendered at 6% Nb+Ti. The inclusions are larger than in the Cu-Cr example, and not quite spherical. The non-zero genus indicates a zone-axis. A description of the panels is given in the caption to figure 10.

[27] Alexandra J. Cackett, Joven J.H. Lim, Przemysław Klupś, Andy J. Bushby, and Christopher D. Hardie. Using spherical indentation to measure the strength of copper-chromium-zirconium. *Journal of Nuclear Materials*, 511:610–616, dec 2018.

[28] R. Lindau, A. Möslang, M. Rieth, M. Klimiankou, E. Materna-Morris, A. Alamo, A.-A. F. Tavassoli, C. Cayron, A.-M. Lancha, P. Fernandez, N. Baluc, R. Schäublin, E. Diegele, G. Filacchioni, J.W. Rensman, B.v.d. Schaaf, E. Lucon, and W. Dietz. Present development status of EUROFER and ODS-EUROFER for application in blanket concepts. *Fusion Engineering and Design*, 75-79:989–996, nov 2005.

[29] Tayebeh Mousavi, Zuliang Hong, Alasdair Morrison, Andrew London, Patrick S Grant, Chris Grovenor, and Susannah C Speller. A new approach to fabricate superconducting NbTi alloys. *Superconductor Science and Technology*, 30(9):094001, jul 2017.

[30] J. Zelenty, A. Dahl, J. Hyde, G.D.W. Smith, and M.P. Moody. Detecting clusters in atom probe data with gaussian mixture models. *Microsc. Microanal.*, 23:269–278, 2017.

VIII. APPENDIX

A. A Maximum Likelihood Denoising (MLD) filter for voxelising atom probe data

Assume that we have some noisy voxelised 3d atom probe data, with the measured concentration on voxel i written as the sum of the expected value plus an error term $\tilde{f}_i = f_i + \delta f_i$. The goal of a filtering algorithm is to find a good approximation for the unknown f_i.

Part of the error δf_i will come from the reconstruction

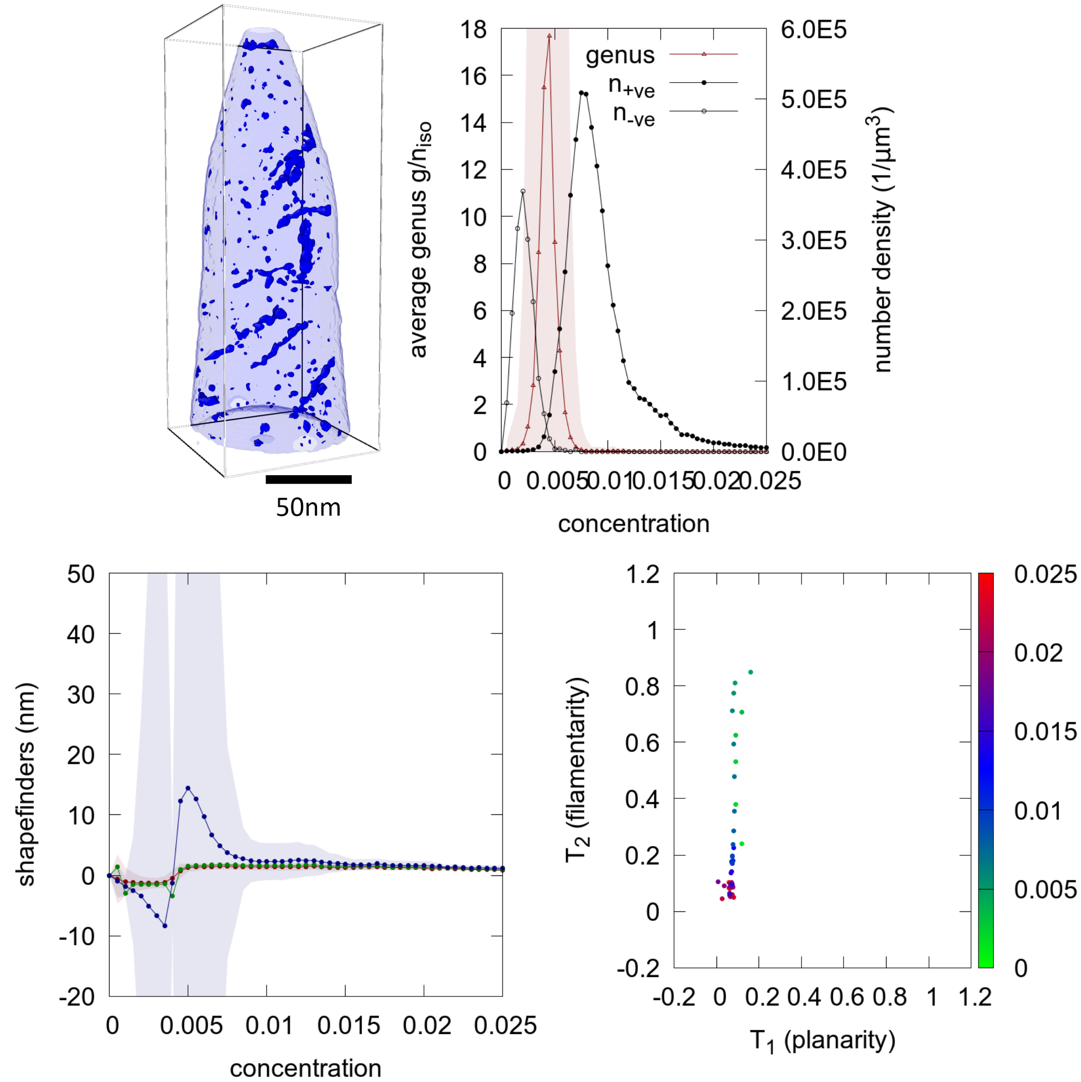

FIG. 12. An analysis of the Mn concentration isosurfaces in an irradiated Eurofer needle. The isosurface is rendered at 1.2% Mn. At 1% concentration, the Mn is segregated to dislocation lines and small spherical regions.

of the position and nature of atoms. Minimising these errors is an active area of ongoing research, but beyond the scope of this paper. A second part of the error will come from sampling errors which we can address here- we have some knowledge of the nature of the statistical distribution of the errors and the physical nature of the concentration field. We will assume that the total number of counts on the detector n_i are available, as are the number of counts of the target atom type k_i, so that we measure $\tilde{f}_i = k_i/n_i$. The total number of counts n_i is likely to be well-approximated by a Poisson process, but as the mean value is dependent on the proximity of surfaces and lensing effects, we can not use this knowledge to much advantage. The recorded count k_i will be well-approximated by a binomial process, B, with a mean $\langle k_i \rangle = n_i f_i$ being the count n_i multiplied by the concentration f_i. We can therefore write down the log-likelihood of having measured $\tilde{f}_i$ as

$$\Lambda = \sum_i \log \left[p\left(\tilde{f}_i | B(n_i, f_i) \right) \right] \tag{14}$$

We will make the *ansatz* that the concentration field f_i is smoothly varying. This is not always going to be true in the case of a sharp interface between phases, but it is also an implicit assumption made by using the Marching Cubes algorithm to construct isosurfaces. Our goal therefore is to find a smooth concentration field f_i which maximises equation 14.

Given input data $\tilde{f}_i$ we can construct smoothed data using a local kernel filter.

$$\tilde{q}_i = \sum_{j \in \mathcal{N}_i} \kappa_{ij} \tilde{f}_j, = \sum_{j \in \mathcal{N}_i} \kappa_{ij} f_j + \sum_{j \in \mathcal{N}_i} \kappa_{ij} \delta f_j. \tag{15}$$

We can identify the second term as the error in the

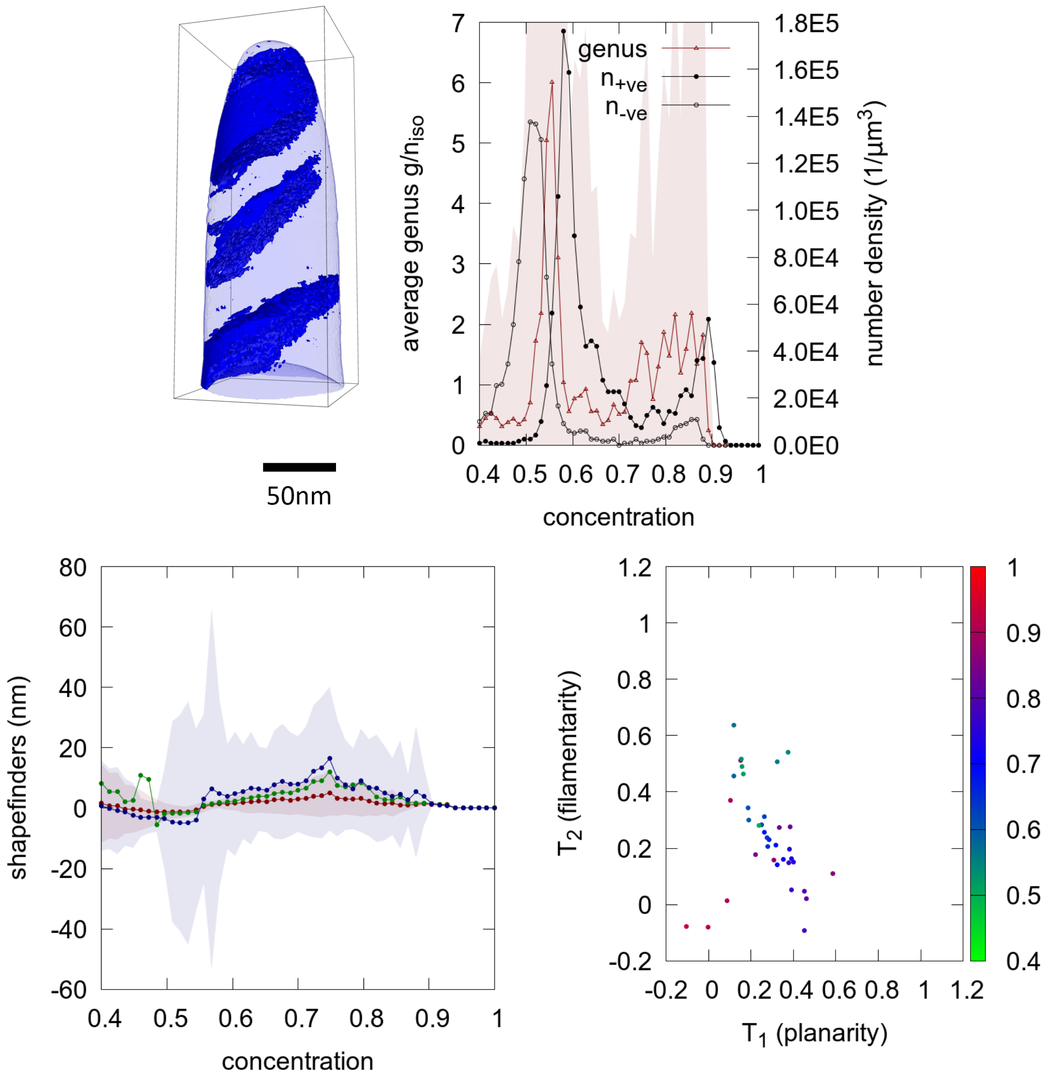

FIG. 13. An analysis of the Ti concentration isosurfaces in an Ni-Ti superalloy. The isosurface is rendered at 75% Ti. Two Ti-phases are present, with 55% and 85% Ti. The high concentration phase shows plate-like structure.

smoothed data estimate, and seek to minimise this error.

$$\delta q_i \equiv \sum_{j\in\mathcal{N}_i} \kappa_{ij}\delta f_j, \tag{16}$$

$$\begin{aligned} \text{so} \quad \langle \delta q_i^2\rangle &= \sum_{j\in\mathcal{N}_i} \kappa_{ij}^2 \langle \delta f_j^2\rangle, \\ &= \sum_{j\in\mathcal{N}_i} \kappa_{ij}^2 \frac{f_j(1-f_j)}{n_j}. \\ &= \sum_{j\in\mathcal{N}_i} \kappa_{ij}^2 \frac{\tilde{f}_j(1-\tilde{f}_j)}{n_j+1}. \end{aligned} \tag{17}$$

where to find the last line we have used the variance of the binomial distribution. Since we also require $\sum_{j\in\mathcal{N}_i}\kappa_{ij} = 1$, equation 17 gives a criterion to optimise the kernel.

We choose a local quadratic kernel, which preserves the second derivative of the concentration function. First Taylor expand a general function about a point to second order

$$q\left(\vec{x}\right) \simeq q_0 + q_0' \cdot \vec{x} + {}^1\!/_2 \vec{x} \cdot q"_0 \vec{x}, \tag{18}$$

which we can fit to the the 26 nearest neighbours on a regular cubic lattice by minimising the function S

$$S = \sum_j w\left(|\vec{x}_j|\right)\left(q\left(\vec{x}_j\right) - \tilde{f}\left(\vec{x}_j\right)\right)^2, \tag{19}$$

where $w(x)$ is a weighting function to be determined.

Writing the neighbours on the six faces as weighted by w_f, the twelve edges as w_e, and the eight corners as w_c, we find S is minimised when

$$\begin{aligned} q_0 = &\frac{(4w_ew_f + 8w_cw_f)}{4\,(3w_ew_f + 8w_fw_c + 4w_cw_e)} \sum_{\text{face,i}} \tilde{f}_j \\ &+ \frac{(-w_ew_f + 4w_cw_e)}{4\,(3w_ew_f + 8w_fw_c + 4w_cw_e)} \sum_{\text{edge,i}} \tilde{f}_j \\ &+ \frac{(-2w_cw_f - 4w_cw_e)}{4\,(3w_ew_f + 8w_fw_c + 4w_cw_e)} \sum_{\text{corner,i}} \tilde{f}_j, \end{aligned} \quad (20)$$

where the notation $\sum_{\text{face,i}} \tilde{f}_j$ denotes a sum over the six voxels on the faces of voxel i. If we then say that the weighting function be a Gaussian, $w(x) = exp(-x^2/2\sigma^2)$, then $w_f = exp(-1/2\sigma^2)$, $w_e = exp(-2/2\sigma^2) = w_f^2$, $w_c = exp(-3/2\sigma^2) = w_f^3$. Note that we require $w_f \leq 1$. Our general 26-neighbour kernel then reduces to

$$\begin{aligned} \kappa_f &= \frac{1}{3 + 2w_f} \\ \kappa_e &= \frac{2w_f - 1}{4(3 + 2w_f)} \\ \kappa_c &= \frac{-w_f}{2(3 + 2w_f)}. \end{aligned} \quad (21)$$

Note that $6\kappa_f + 12\kappa_e + 8\kappa_c = 1$. We can therefore minimise equation 17, by minimising $\langle \delta q_i^2 \rangle$ with respect to w_f.

After some manipulations, this gives the closed form end result

$$w_f = \min\left(1, \frac{2\sum_{\text{edge,i}} \frac{\tilde{f}_j(1-\tilde{f}_j)}{n_j} + 8\sum_{\text{face,i}} \frac{\tilde{f}_j(1-\tilde{f}_j)}{n_j}}{3\sum_{\text{corner,i}} \frac{\tilde{f}_j(1-\tilde{f}_j)}{n_j} + 4\sum_{\text{edge,i}} \frac{\tilde{f}_j(1-\tilde{f}_j)}{n_j}}\right) \quad (22)$$

which we can substitute into equation 21 to find a kernel for each voxel. This gives an expected value $\tilde{q}_i$ on each voxel, given the local variation,

$$\tilde{q}_i = \sum_{\text{face,i}} \kappa_f \tilde{f}_j + \sum_{\text{edge,i}} \kappa_e \tilde{f}_j + \sum_{\text{corner,i}} \kappa_c \tilde{f}_j. \quad (23)$$

Note that there is no guarantee that atom count is conserved,[2] as $\sum_i \tilde{q}_i n_i \neq \sum_i \tilde{f}_i n_i$. Instead we can try

$$f_i \simeq \tilde{f}_i + \alpha_i(\tilde{q}_i - \tilde{f}_i) + \beta_i, \quad (24)$$

where $\alpha_i = 1/(n_i + 1)$ is an empirical weighting to allow voxels with a high number count to resist alteration. β_i is selected such that $\sum_i f_i n_i = \sum_i \tilde{f}_i n_i$, subject to the condition $0 \leq f_i \leq 1$. We can then compute the log-likelihood of the measurement (equation 14). If the log-likelihood is increasing, we can iterate, using f_i in place of $\tilde{f}_i$ to compute the kernel (equations 22,21), then using equations 23,24 to update f_i again, until the maximum log-likelihood is found. By this iterative scheme we find a smoothed concentration field f_i which preserves the atom count and maximises the likelihood of having measured $\tilde{f}_i$.

B. Surface refinement

There is an extensive literature on generating 'good' surfaces using refinements of the MC algorithm, and it is beyond the scope of this paper to review them. In this work we use an inexpensive refinement to the triangulated surface to improve the meshing. After the initial triangle set is produced with a tri-linear interpolation, we exploit the fact that we also maintain the phase field in a tri-cubic approximation to refine the mesh. If the field locally is described by

$$f(\vec{x}) = f_0 + \nabla f \cdot \vec{x} + \frac{1}{2}\vec{x} \cdot G\vec{x} + ..., \quad (25)$$

where $G = \nabla\nabla f$ is a matrix of second derivatives, then the point $f(\vec{x} + \lambda\nabla f)$ is a better estimate for the location of the isosurface $f = f_0$, where

$$\begin{aligned} \lambda = &-\frac{\nabla f \cdot \nabla f}{\nabla f \cdot G\nabla f} \\ &\pm \frac{1}{\nabla f \cdot G\nabla f}\sqrt{(\nabla f \cdot \nabla f)^2 - 2\nabla f \cdot G\nabla f\,(f(\vec{x}) - f_0)} \end{aligned} \quad (26)$$

The sign is chosen to minimise the magnitude of λ. We refine the surface by introducing new vertices at the midpoint of each triangle edge, and using equation 26 to take vertex to the isosurface. This quadruples the number of triangles, improving the surface integrals, and is very quick as the position and connectivity of the new vertices can be deduced from the old vertices. As an example consider an octahedral isosurface which is the smallest MC meshing for a sphere radius $R << a$ (see figure 14), and is a worst-case scenario for the accurate representation of the true surface. The volume and surface area of an octahedron are $V = 4R^3/3 = 1.333R^3$ and $S = 4\sqrt{3}R^2 = 6.928R^2$, compared to the true values for the sphere $V = (4\pi/3)R^3/3 = 4.189R^3$ and $S = 4\pi R^2 = 12.566R^2$. Note that the octahedral estimates are very low. With our correction, inflating the midpoints from $[R/2, R/2, 0]$ positions to the isosurface at $[R/\sqrt{2}, R/\sqrt{2}, 0]$ positions, the volume and surface area increase to $V = (2 + 2\sqrt{2}/3)R^3 = 2.943R^3$, $S = 12\sqrt{7/4 - \sqrt{2}}R^2 + 2\sqrt{3} = 10.418R^2$. The volume and surface area errors have halved, from -68% to -30%, and -45% to -17% respectively. Note that this systematic underestimate of volume and surface area are characteristic of convex triangulated surfaces.

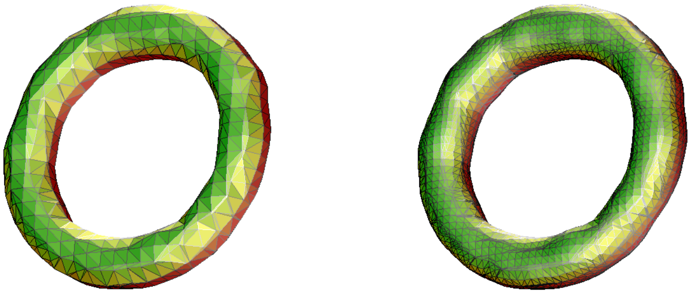

FIG. 14. Simple mesh refinement by inflating the midpoint of each original triangle to the isosurface. Left: The torus concentration field defined in section V, at a concentration isolevel of $f = 0.5$. Right: a simple mesh refinement takes the midpoints of each triangle edge and pushes them to the isosurface.

---

[2] Note that if a simple Gaussian smoothing kernel were used to find a smoothed concentration field as $\tilde{q}_i = \sum_j \kappa_{\mathrm{Gauss},j} \tilde{f}_j$, we would expect to preserve the summed concentration $\sum_i \tilde{q}_i$, but not necessarily atom count $\sum_i \tilde{q}_i n_i$.